Wave-equation Hessian by phase encoding

Yaxun Tang

ABSTRACT

I present a method for computing wave-equation Hessian operators, also known as resolution functions or point-spread functions, under the Born approximation. The proposed method modifies the original explicit Hessian formula, enabling efficient computation of the operator. A particular advantage of this method is that it reduces or eliminates on-disk storage of Green's functions. The modifications, however, also introduce undesired cross-talk artifacts. I examine two different phase-encoding schemes, namely, plane-wave phase encoding and random phase encoding, to suppress the cross-talk. I apply the Hessian operator obtained by using random phase encoding to the Sigsbee2A synthetic data set, where a better subsalt image with higher resolution is obtained.

INTRODUCTION

Migration is an important tool for imaging subsurface structures using reflection seismic data. The classic imaging principle for shot-based migration states that reflectors are located where the forward-propagated source wavefield correlates with the backward-propagated receiver wavefield (Claerbout, 1971). However, this imaging principle is only the adjoint of the forward Born modeling operator (Lailly, 1983), which provides reliable structural information of the subsurface, but distorts the amplitude of the reflectors because of the non-unitary nature of the Born modeling operator. To improve relative amplitude behavior, the imaging problem can be formulated as an inverse problem based on the minimization of a least-squares functional. The inverse problem can be formulated either in the data space (Lailly, 1983; Tarantola, 1984; Nemeth et al., 1999; Clapp, 2005) or in the model space (Beylkin, 1985; Chavent and Plessix, 1999; Plessix and Mulder, 2004; Valenciano et al., 2006; Yu et al., 2006). The data-space approach can be solved iteratively using the gradient-based method (Nemeth et al., 1999; Clapp, 2005) without explicit construction of the Hessian, the matrix of the second derivatives of the error functional with respect to the model parameters. The iterative solving, however, is relatively costly and converges very slowly.

On the other hand, the model-space approach requires explicitly constructing the Hessian and applying its pseudo-inverse to the migrated image. The full Hessian of the least-squares functional is too big and expensive to be computed in practical applications; hence Chavent and Plessix (1999); Plessix and Mulder (2004) approximate it by a diagonal matrix. In the case of high-frequency asymptotics, and with

an infinite aperture, the Hessian is diagonal in most cases (Beylkin, 1985). For a finite range of frequencies and limited acquisition geometry, however, the Hessian is no longer diagonal and not even diagonally dominated (Chavent and Plessix, 1999; Pratt et al., 1998; Plessix and Mulder, 2004; Valenciano et al., 2006). It has been shown by Valenciano et al. (2006) that, in areas of poor illumination, e.g., subsalt regions, the Hessian's main diagonal energy is smeared along its off-diagonals. Therefore, the migrated image pre-multiplied by a diagonal matrix cannot perfectly recover the amplitude information, especially in poorly illuminated areas. That's why Valenciano et al. (2006) suggest computing a limited number of the Hessian off-diagonals to compensate for poor illumination and improve the inversion result. However, computing the Hessian off-diagonals, even for a limited number, is very expensive by direct implementation of the explicit Hessian formula. A huge number of Green's functions (easily several hundred terabytes for a typical 3-D survey) must be pre-computed and stored and then retrieved from the disk to generate the Hessian. Such operations not only require high-volume storage, but also high-speed I/O and network. Though computer speed continues to improve rapidly, computing such a huge matrix is still a challenge.

To make the Hessian computation more affordable, I describe a method based on the phase-encoding technique. In this method, the original explicit Hessian formula is slightly modified to enable efficient computation of the Hessian operator. The proposed method makes the Hessian computation similar to the shot-profile migration but with slightly modified imaging conditions. The new method eliminates the need to pre-compute and store Green's functions, but it also introduces cross-talk artifacts. I examine two phase-encoding schemes, plane-wave phase encoding and random phase encoding to attenuate the cross-talk.

This paper is organized as follows. First, I briefly review the theory of formulating the inverse problem in the model space. Then I discuss how the explicit Hessian can be efficiently computed using phase encoding. Finally, I apply the phase-encoded Hessian to the Sigsbee2A model, where a better subsalt image with higher resolution is obtained.

LEAST-SQUARES HESSIAN

Forward modeling using conventional two-way acoustic wave equation is a non-linear process that generates not only primaries, but also multiples. In imaging, however, multiples are often treated as noise and we mainly use primary information to image the subsurface. Primaries can be modeled using the Born approximation of the non-linear two-way wave equation by assuming a smooth background slowness field and small slowness perturbations. By making such assumptions, we can synthesize primaries by using the Born modeling equation as follows:

$$d(\mathbf{r}_k, \mathbf{s}_i, \omega) = \omega^2 \sum_{l=1}^{L} f_s(\omega) G_i(\mathbf{s}_i, \mathbf{x}_l, \omega) G_i(\mathbf{x}_l, \mathbf{r}_k, \omega) m(\mathbf{x}_l), \tag{1}$$

where $d(\mathbf{r}_k, \mathbf{s}_i, \omega)$ is the modeled seismic data for receiver location $\mathbf{r}_k$ $(k = 1, \cdots, M)$ and shot location $\mathbf{s}_i$ $(i = 1, \cdots, N)$ for a single frequency ω, $f_s(\omega)$ is the source signature. $m(\mathbf{x}_l)$ $(l = 1, \cdots, L)$ is the reflectivity at $\mathbf{x}_l$ in the subsurface, $G_i(\mathbf{s}_i, \mathbf{x}_l, \omega)$ is the monochromatic Green's function from the source $\mathbf{s}_i$ to the image point $\mathbf{x}_l$ for the ith shot, and $G_i(\mathbf{x}_l, \mathbf{r}_k, \omega)$ is the monochromatic Green's function from the image point $\mathbf{x}_l$ to the receiver $\mathbf{r}_k$ for the ith shot.

Given the linear modeling equation 1, the adjoint equation is obtained by simply transposing and taking the complex conjugate of the modeling operator:

$$m_{mig}(\mathbf{x}_l) = \sum_{\omega} \omega^2 \sum_{i=1}^{N} f_s'(\omega) G_i'(\mathbf{s}_i, \mathbf{x}_l, \omega) \sum_{k=1}^{M} G_i'(\mathbf{x}_l, \mathbf{r}_k, \omega) d(\mathbf{r}_k, \mathbf{s}_i, \omega), \tag{2}$$

where $'$ stands for the complex conjugate. Equation 2 is the standard wave-equation shot-profile migration, which has been widely used in the industry. Migration positions the reflectors correctly in the subsurface. The amplitude information, however, is not well preserved: since the Born modeling operator (equation 1) is non-unitary, its adjoint, i.e., the migration operator (equation 2) is not the true inverse of the modeling operator. To better recover the amplitudes, we need to go beyond migration by formulating the imaging problem as an inverse problem, which enables us to find a generalized inverse of the modeling operator.

In using inverse theory, we first formulate an objective function in the least-square sense as follows:

$$F(\mathbf{m}) = \frac{1}{2} \sum_{\omega} \sum_{k=1}^{M} \sum_{i=1}^{N} \left| d(\mathbf{r}_k, \mathbf{s}_i, \omega) - d_{obs}(\mathbf{r}_k, \mathbf{s}_i, \omega) \right|^2, \tag{3}$$

where $d(\mathbf{r}_k, \mathbf{s}_i, \omega)$ represents the modeled data by using equation 1, and $d_{obs}(\mathbf{r}_k, \mathbf{s}_i, \omega)$ represents the observed data. Now the goal is to find a model $\mathbf{m} = (m(\mathbf{x}_1), \cdots, m(\mathbf{x}_L))$ that best fits the recorded data $\mathbf{d}_{obs}$ in the least-square sense. Equation 3 can also be written in a more compact form as follows:

$$F(\mathbf{m}) = ||\mathbf{d} - \mathbf{d}_{obs}||_2 = ||\mathbf{L}\mathbf{m} - \mathbf{d}_{obs}||_2, \tag{4}$$

where $\mathbf{L}$ is the forward modeling operator defined in equation 1, and $||\cdot||_2$ stands for the L_2 norm. Equation 4 can be solved directly using the gradient-based methods (Nemeth et al., 1999; Clapp, 2005). The main obstacle to its wide use is its cost; three wavefield propagations are required within each iteration, making it impractical for large-scale problems. Another drawback is its relatively slow convergence rate, since only the gradient information of the objective function F is used in the optimization process.

Instead of solving equation 4 directly in the data space, we can reformulate it and solve it in the model space. Because $\mathbf{L}$ is a linear operator, F is a quadratic function. Its minimum is obtained when $\mathbf{m}$ satisfies:

$$\mathbf{m} = \mathbf{H}^{-1}\mathbf{L}'\mathbf{d}_{obs}, \tag{5}$$

where $\mathbf{H} = \mathbf{L}'\mathbf{L}$ is the Hessian operator. The Hessian provides the curvature information of the objective function F. We can rewrite equation 5 by recognizing that $\mathbf{L}'\mathbf{d}_{obs}$ is the migrated image $\mathbf{m}_{mig}$ (equation 2)

$$\mathbf{Hm} = \mathbf{m}_{mig}. \tag{6}$$

Now we can formulate our new objective function as follows:

$$J(\mathbf{m}) = ||\mathbf{Hm} - \mathbf{m}_{mig}||_2. \tag{7}$$

Equation 7 says that once we explicitly compute the Hessian operator $\mathbf{H}$, we can use the linear conjugate-gradient or any other method to minimize the new objective function J defined in equation 7.

Equation 7 is mathematically equivalent to equation 3, with the only difference being that the former is formulated in the model space, while the latter in the data space. The main advantage of model-space approach is that we can invert the model parameters in a target-oriented fashion (Valenciano et al., 2006), which substantially reduces the size of the problem. For example, we can choose to invert only areas of particular interest, such as subsalt regions, where reservoirs are often located. In fact, the model-space approach divides the original problem defined by equation 3 into two stages: computing the explicit Hessian and minimizing the objective function J. Since minimizing the objective function J is trivial once the Hessian is obtained, various regularization schemes can be easily tried to improve the inversion result without any additional cost. This is another important advantage of formulating inverse problem in the model space.

The Hessian can be obtained by taking the second derivative of the objective function F with respect to the model parameters, the formula is given as follows (see Appendix A for derivation):

$$H(\mathbf{x}_p, \mathbf{x}_q) = \sum_{\omega} \omega^4 \sum_{i=1}^{N} |f_s(\omega)|^2 G_i(\mathbf{s}_i, \mathbf{x}_p, \omega) G_i'(\mathbf{s}_i, \mathbf{x}_q, \omega) \sum_{k=1}^{M} G_i(\mathbf{r}_k, \mathbf{x}_p, \omega) G_i'(\mathbf{r}_k, \mathbf{x}_q, \omega) \tag{8}$$

Hereafter, I call $H(\mathbf{x}_p, \mathbf{x}_q)$ in equation 8 the exact Hessian, since it is derived strictly from the least-squares functional F. It is cumbersome and very expensive to compute the exact Hessian by directly implementing the above equation, because large storage of Green's function is needed. In the subsequent sections, I introduce an alternative method based on phase encoding for computing the Hessian operator, which reduces the computational requirement. As I will demonstrate, by using this approach, we do not need to save any Green's functions, and the cost for computing the Hessian is also significantly reduced.

PHASE-ENCODED HESSIAN

Encoding of the receiver-side Green's functions

Suppose we have the following function:

$$\begin{aligned}\tilde{H}(\mathbf{x}_p,\mathbf{x}_q) &= \sum_{\omega}\omega^4\sum_{i=1}^{N}|f_s(\omega)|^2 G_i(\mathbf{s}_i,\mathbf{x}_p,\omega)G_i'(\mathbf{s}_i,\mathbf{x}_q,\omega)\times \\ &\quad \sum_{u=1}^{M}G_i(\mathbf{r}_u,\mathbf{x}_p,\omega)\alpha_u(\omega)\sum_{v=1}^{M}G_i'(\mathbf{r}_v,\mathbf{x}_q,\omega)\alpha_v'(\omega),\end{aligned} \tag{9}$$

where we introduce an extra summation $\sum_{v=1}^{M}$ for the receiver-side Green's functions; $\alpha_u(\omega)$ and $\alpha_v(\omega)$ are some weighting functions to be specified later. Equation 9 can be directly implemented by storing the Green's functions, just as with the direct implementation of equation 8. However, equation 9 offers more flexibility and can be very efficiently implemented without explicitly saving the Green's functions.

With the extra summation, the term $\sum_{u=1}^{M}G_i(\mathbf{r}_u,\mathbf{x}_p,\omega)\alpha_u(\omega)$ can now be seen as the extrapolated wavefield at the image point $\mathbf{x}_p$, using the composite source as the source function ($f_c(\mathbf{r}_u,\omega)=\alpha_u(\omega),\ u=1,\cdots,M$). The same thing holds for the other summation term $\sum_{v=1}^{M}G_i'(\mathbf{r}_v,\mathbf{x}_q,\omega)\alpha_v'(\omega)$, except that it is the complex conjugate of the extrapolated wavefield at the image point $\mathbf{x}_q$. To make it clearer, we define the receiver wavefield $R_i(\mathbf{x},\omega)$ corresponding to the receiver composite source for the ith shot gather as

$$R_i(\mathbf{x},\omega)=\sum_{u=1}^{M}G_i(\mathbf{r}_u,\mathbf{x},\omega)\alpha_u(\omega), \tag{10}$$

and the source wavefield corresponding to a point source located at $\mathbf{s}_i$ on the surface as

$$S_i(\mathbf{x},\omega)=f_s(\omega)G_i(\mathbf{s}_i,\mathbf{x},\omega). \tag{11}$$

Substituting equations 10 and 11 into equation 9 leads to

$$\tilde{H}(\mathbf{x}_p,\mathbf{x}_q)=\sum_{\omega}\omega^4\sum_{i=1}^{N}S_i(\mathbf{x}_p,\omega)S_i'(\mathbf{x}_q,\omega)R_i(\mathbf{x}_p,\omega)R_i'(\mathbf{x}_q,\omega), \tag{12}$$

which means $\tilde{H}(\mathbf{x}_p,\mathbf{x}_q)$ can be computed by cross-correlating the source and receiver wavefields with their shifted complex conjugates ($\mathbf{x}_q$ is the neighborhood point around $\mathbf{x}_p$). It is similar to the wave-equation shot-profile migration process, except the imaging condition is slightly modified. In other words, we do not have to save the Green's functions. Instead, we can replace each shot gather with composite sources, then extrapolate it into the subsurface and use the imaging condition defined in equation 12 to generate $\tilde{H}(\mathbf{x}_p,\mathbf{x}_q)$. This process is efficient because multiple Green's functions are computed at the same time during the wavefield extrapolation.

It can be shown that after some simple algebraic manipulation, equation 9 can be rewritten as follows:

$$\begin{aligned}\tilde{H}(\mathbf{x}_p,\mathbf{x}_q) &= \sum_{\omega}\omega^4\sum_{i=1}^{N}|f_s(\omega)|^2 G_i(\mathbf{s}_i,\mathbf{x}_p,\omega)G_i'(\mathbf{s}_i,\mathbf{x}_q,\omega)\times \\ &\quad \sum_{k=1}^{M} G_i(\mathbf{r}_k,\mathbf{x}_p,\omega)G_i'(\mathbf{r}_k,\mathbf{x}_q,\omega)|\alpha_k(\omega)|^2 + \\ &\quad \sum_{\omega}\omega^4\sum_{i=1}^{N}|f_s(\omega)|^2 G_i(\mathbf{s}_i,\mathbf{x}_p,\omega)G_i'(\mathbf{s}_i,\mathbf{x}_q,\omega)\times \\ &\quad \sum_{u=1}^{M}\sum_{v=1(u\neq v)}^{M} G_i(\mathbf{r}_u,\mathbf{x}_p,\omega)G_i'(\mathbf{r}_v,\mathbf{x}_q,\omega)\alpha_u(\omega)\alpha_v'(\omega). \qquad (13)\end{aligned}$$

If we let the weighting function $\alpha_k(\omega)$ satisfy $|\alpha_k(\omega)| = 1$, the first term in equation 13 becomes the exact Hessian $H(\mathbf{x}_p,\mathbf{x}_q)$; however, the second term is the undesired cross-talk from the cross-correlations among different receiver-side Green's functions.

$$\begin{aligned}\tilde{H}(\mathbf{x}_p,\mathbf{x}_q) &= H(\mathbf{x}_p,\mathbf{x}_q) + \\ &\quad \sum_{\omega}\omega^4\sum_{i=1}^{N}|f_s(\omega)|^2 G_i(\mathbf{s}_i,\mathbf{x}_p,\omega)G_i'(\mathbf{s}_i,\mathbf{x}_q,\omega)\times \\ &\quad \sum_{u=1}^{M}\sum_{v=1(u\neq v)}^{M} G_i(\mathbf{r}_u,\mathbf{x}_p,\omega)G_i'(\mathbf{r}_v,\mathbf{x}_q,\omega)\alpha_u(\omega)\alpha_v'(\omega) \qquad (14)\end{aligned}$$

Simultaneous encoding of the source-side and receiver-side Green's functions

We can further encode the source-side Green's function by synthesizing composite sources from the source locations. For simplicity, we assume ocean bottom cable (OBC) or land acquisition geometry, where all the shots share the same receiver array. Therefore we have the following relations:

$$G_i(\mathbf{s}_i,\mathbf{x},\omega) = G(\mathbf{s}_i,\mathbf{x},\omega) \qquad (15)$$

$$G_i(\mathbf{r}_k,\mathbf{x},\omega) = G(\mathbf{r}_k,\mathbf{x},\omega). \qquad (16)$$

Then the following function can be constructed:

$$\begin{aligned}\tilde{\tilde{H}}(\mathbf{x}_p,\mathbf{x}_q) &= \sum_{\omega}\omega^4|f_s(\omega)|^2\sum_{i=1}^{N} G(\mathbf{s}_i,\mathbf{x}_p,\omega)\beta_i(\omega)\sum_{j=1}^{N} G'(\mathbf{s}_j,\mathbf{x}_q,\omega)\beta_j'(\omega)\times \\ &\quad \sum_{u=1}^{M} G(\mathbf{r}_u,\mathbf{x}_p,\omega)\alpha_u(\omega)\sum_{v=1}^{M} G'(\mathbf{r}_v,\mathbf{x}_q,\omega)\alpha_v'(\omega), \qquad (17)\end{aligned}$$

where we introduce two extra summations: $\sum_{j=1}^{N}$ for the source-side Green's function and $\sum_{v=1}^{M}$ for the receiver-side Green's function. Let us once again define the composite source wavefield $S(\mathbf{x},\omega)$ and composite receiver wavefield $R(\mathbf{x},\omega)$ as follows:

$$S(\mathbf{x},\omega) = f_s(\omega)\sum_{i=1}^{N} G(\mathbf{s}_i,\mathbf{x},\omega)\beta_i(\omega), \tag{18}$$

and

$$R(\mathbf{x},\omega) = \sum_{u=1}^{M} G(\mathbf{r}_u,\mathbf{x},\omega)\alpha_u(\omega). \tag{19}$$

Substituting equations 18 and 19 into equation 17 leads to

$$\tilde{\tilde{H}}(\mathbf{x}_p,\mathbf{x}_q) = \sum_{\omega} \omega^4 S(\mathbf{x}_p,\omega)S'(\mathbf{x}_q,\omega)R(\mathbf{x}_p,\omega)R'(\mathbf{x}_q,\omega). \tag{20}$$

Equation 20 tells us that to compute the simultaneously encoded Hessian $\tilde{\tilde{H}}(\mathbf{x}_p,\mathbf{x}_q)$ for OBC or land acquisition geometry, only two wavefield propagations are required: one for the composite source wavefield defined by equation 18, and the other for the composite receiver wavefield defined by equation 19. We may rewrite equation 17 as

$$\begin{aligned}
\tilde{\tilde{H}}(\mathbf{x}_p,\mathbf{x}_q) \;=\; & \sum_{\omega} \omega^4 |f_s(\omega)|^2 \sum_{i=1}^{N} G(\mathbf{s}_i,\mathbf{x}_p,\omega)G'(\mathbf{s}_i,\mathbf{x}_q,\omega)|\beta_i(\omega)|^2 \times \\
& \sum_{k=1}^{M} G(\mathbf{r}_k,\mathbf{x}_p,\omega)G'(\mathbf{r}_k,\mathbf{x}_q,\omega)|\alpha_k(\omega)|^2 + \\
& \sum_{\omega} \omega^4 |f_s(\omega)|^2 \sum_{i=1}^{N} \sum_{j=1(i\neq j)}^{N} G(\mathbf{s}_i,\mathbf{x}_p,\omega)G'(\mathbf{s}_j,\mathbf{x}_q,\omega)\beta_i(\omega)\beta'_j(\omega) \times \\
& \sum_{u=1}^{M} \sum_{v=1(u\neq v)}^{M} G(\mathbf{r}_u,\mathbf{x}_p,\omega)G'(\mathbf{r}_v,\mathbf{x}_q,\omega)\alpha_u(\omega)\alpha'_v(\omega).
\end{aligned} \tag{21}$$

If we can choose proper weighting functions $\alpha_k(\omega)$ and $\beta_i(\omega)$ such that $|\alpha_k(\omega)| = 1$ and $|\beta_i(\omega)| = 1$, then the first term in equation 21 becomes the exact Hessian $H(\mathbf{x}_p,\mathbf{x}_q)$, and the second term becomes the undesired cross-talk:

$$\begin{aligned}
\tilde{\tilde{H}}(\mathbf{x}_p,\mathbf{x}_q) \;=\; & H(\mathbf{x}_p,\mathbf{x}_q) + \\
& \sum_{\omega} \omega^4 |f_s(\omega)|^2 \sum_{i=1}^{N} \sum_{j=1(i\neq j)}^{N} G(\mathbf{s}_i,\mathbf{x}_p,\omega)G'(\mathbf{s}_j,\mathbf{x}_q,\omega)\beta_i(\omega)\beta'_j(\omega) \times \\
& \sum_{u=1}^{M} \sum_{v=1(u\neq v)}^{M} G(\mathbf{r}_u,\mathbf{x}_p,\omega)G'(\mathbf{r}_v,\mathbf{x}_q,\omega)\alpha_u(\omega)\alpha'_v(\omega).
\end{aligned} \tag{22}$$

From equations 14 and 22, we face a similar situation encountered in phase-encoding migration (Romero et al., 2000); i.e., our exact Hessian is contaminated

by cross-talk artifacts, so we seek to define weighting functions $\alpha_k(\omega)$ and $\beta_i(\omega)$ that attenuate the cross-talk as much as possible. In the next two sections, I examine two different phase-encoding schemes to attenuate that cross-talk, namely, plane-wave phase encoding and random phase encoding.

PLANE-WAVE PHASE ENCODING

Let us first encode only the receiver-side Green's functions. Suppose we choose the weighting functions to be

$$\alpha_k(\omega) = \alpha_k(p_r, \omega) = A_r(\omega) \mathrm{e}^{\iota\omega p_r(\mathbf{r}_k - \mathbf{r}_0)}, \tag{23}$$

which is the known plane-wave phase-encoding function (Whitmore, 1995; Liu et al., 2006), where $A_r(\omega)$ is a real function depending upon the angular frequency ω, $\iota = \sqrt{-1}$; the vector $\mathbf{r}_0$ is some reference location, and p_r is the ray-parameter at the surface. Here we limit our discussion to 2-D, so p_r is a scalar, but it is very straightforward to extend the analysis to 3-D. As proved by Liu et al. (2006), summing an infinite number of plane waves ranging from $p_r = -\infty$ to $+\infty$ completely attenuates the cross-talk in the plane-wave migration, and the final migration result is exactly equivalent to the standard shot-profile migration result. The same property holds here in the scenario of Hessian computation, as proved in Appendix B: stacking over p_r and choosing $A_r(\omega)$ to satisfy $|\omega|^{-1} A_r^2(\omega) = 1$, the approximate Hessian $\tilde{H}(\mathbf{x}_p, \mathbf{x}_q, p_r)$ converges to the exact Hessian $H(\mathbf{x}_p, \mathbf{x}_q)$:

$$\sum_{p_r=-\infty}^{+\infty} \tilde{H}(\mathbf{x}_p, \mathbf{x}_q, p_r) = H(\mathbf{x}_p, \mathbf{x}_q). \tag{24}$$

Similarly, in the case of simultaneous encoding, we can choose the weighting functions $\alpha_k(\omega)$ and $\beta_i(\omega)$ to be

$$\alpha_k(\omega) = \alpha_k(p_r, \omega) = A_r(\omega) \mathrm{e}^{\iota\omega p_r(\mathbf{r}_k - \mathbf{r}_0)} \tag{25}$$

$$\beta_i(\omega) = \beta_i(p_s, \omega) = A_s(\omega) \mathrm{e}^{\iota\omega p_s(\mathbf{s}_i - \mathbf{s}_0)}, \tag{26}$$

where p_r and p_s are the receiver-side and source-side plane-wave ray parameters. Once again, the analysis is limited to 2-D, so p_r and p_s are scalars. The vectors $\mathbf{r}_0$ and $\mathbf{s}_0$ are some reference locations for receiver and source plane waves respectively. $A_r(\omega)$ and $A_s(\omega)$ are real functions. Similar to the analysis in Appendix B, Appendix C proves that by stacking over p_s and p_r and choosing $A_s(\omega)$ and $A_r(\omega)$ to satisfy $|\omega|^{-1} A_s^2(\omega) = 1$ and $|\omega|^{-1} A_r^2(\omega) = 1$, the final stacking result is equivalent to the exact Hessian:

$$\sum_{p_s=-\infty}^{+\infty} \sum_{p_r=-\infty}^{+\infty} \tilde{\tilde{H}}(\mathbf{x}_p, \mathbf{x}_q, p_s, p_r) = H(\mathbf{x}_p, \mathbf{x}_q). \tag{27}$$

RANDOM PHASE ENCODING

Instead of using the plane-wave encoding phase function, we can use random phases to disperse unwanted cross-terms. By doing so, we do not need to stack over p_r or p_s to attenuate the cross-talk, so the cost is significantly reduced. To encode only the receiver-side Green's function, we can choose the weighting function in equation 13 to be

$$\begin{aligned} \alpha_u(\omega) &= \mathrm{e}^{\iota\gamma_u(\omega)} \\ \alpha_v(\omega) &= \mathrm{e}^{\iota\gamma_v(\omega)}. \end{aligned}$$

Since $|e^{\iota\gamma_u(\omega)}| = 1$, then equation 13 becomes

$$\begin{aligned} \tilde{H}(\mathbf{x}_p, \mathbf{x}_q) &= H(\mathbf{x}_p, \mathbf{x}_q) + \\ &\sum_{\omega} \omega^4 \sum_{i=1}^{N} |f_s(\omega)|^2 G_i(\mathbf{s}_i, \mathbf{x}_p, \omega) G_i'(\mathbf{s}_i, \mathbf{x}_q, \omega) \times \\ &\sum_{u=1}^{M} \sum_{v=1(u\neq v)}^{M} G_i(\mathbf{r}_u, \mathbf{x}_p, \omega) G_i'(\mathbf{r}_v, \mathbf{x}_q, \omega) \mathrm{e}^{\iota(\gamma_u(\omega) - \gamma_v(\omega))}. \end{aligned} \tag{28}$$

Suppose we choose the phase function $\gamma_r(\omega) = \gamma_u(\omega) - \gamma_v(\omega)$ to be a sequence of random numbers between 0 and 2π. When we sum over ω to generate the final result, the phases will not agree, and consequently, the cross-talk will be attenuated. To maximize the phase differences from each frequency, a uniformly distributed random sequence could be used.

Similarly, for the case of simultaneous encoding, we choose the weighting functions in equation 21 to be

$$\begin{aligned} \alpha_u(\omega) &= \mathrm{e}^{\iota\gamma_u(\omega)} \\ \alpha_v(\omega) &= \mathrm{e}^{\iota\gamma_v(\omega)} \\ \beta_i(\omega) &= \mathrm{e}^{\iota\gamma_i(\omega)} \\ \beta_j(\omega) &= \mathrm{e}^{\iota\gamma_j(\omega)}. \end{aligned}$$

Then equation 21 becomes

$$\begin{aligned} \tilde{\tilde{H}}(\mathbf{x}_p, \mathbf{x}_q) &= H(\mathbf{x}_p, \mathbf{x}_q) + \\ &\sum_{\omega} \omega^4 |f_s(\omega)|^2 \sum_{i=1}^{N} \sum_{j=1(i\neq j)}^{N} G(\mathbf{s}_i, \mathbf{x}_p, \omega) G'(\mathbf{s}_j, \mathbf{x}_q, \omega) e^{\iota(\gamma_i(\omega) - \gamma_j(\omega))} \times \\ &\sum_{u=1}^{M} \sum_{v=1(u\neq v)}^{M} G(\mathbf{r}_u, \mathbf{x}_p, \omega) G'(\mathbf{r}_v, \mathbf{x}_q, \omega) e^{\iota(\gamma_u(\omega) - \gamma_v(\omega))}. \end{aligned} \tag{29}$$

By choosing phase functions $\gamma_s(\omega) = \gamma_i(\omega) - \gamma_j(\omega)$ and $\gamma_r(\omega) = \gamma_u(\omega) - \gamma_v(\omega)$ to be uniformly distributed random sequences, we maximize the attenuation of the cross-talk in equation 29 when stacking over frequencies.

COST COMPARISON

In this section, I compare the cost for different methods to have an idea of the savings generated by using the phase-encoding method. As discussed before, Hessian computation mainly contains two parts: wavefield propagation (Green's functions) and cross-correlation among different Green's functions. Since the cross-correlation parts are similar for methods with or without phase encoding, I will compare the cost for the first part, i.e, wavefield propagation for Green's functions.

Let us assume a 3-D seismic survey that has N_s shots in total, covering a surface area that can be divided into $N_x \times N_y$ cells. Table 1 illustrates the number of wavefield propagations and the size of Green's functions for an image cube with the size $N'_x \times N'_y \times N'_z$ for different methods. N_ω is the number of frequencies of the wavefield, $N_{p_{s_x}}$ and $N_{p_{s_y}}$ are the source ray parameters for the in-line and cross-line directions, and $N_{p_{r_x}}$ and $N_{p_{r_y}}$ are the receiver ray parameters for the in-line and cross-line directions respectively. For simultaneous encoding methods, OBC or land recording geometry has been assumed.

Table 1: Comparison of the costs for different methods

Method	Wavefield propagations	Size of Green's functions
direct computation	$N_x N_y N_\omega$	$N_x N_y N'_x N'_y N'_z N_\omega$
plane-wave, receiver-side	$(1 + N_{p_{r_x}} N_{p_{r_y}}) N_s N_\omega$	0
plane-wave, simultaneous	$(N_{p_{s_x}} N_{p_{s_y}} + N_{p_{r_x}} N_{p_{r_y}}) N_\omega$	0
random, receiver-side	$2 N_s N_\omega$	0
random, simultaneous	$2 N_\omega$	0

Considering that $N_{p_{s_x}}, N_{p_{s_y}}, N_{p_{r_x}}$ and $N_{p_{r_y}}$ are usually much smaller than N_x and N_y in practice, the phase-encoding methods generally need far fewer wavefield propagations. The most efficient method would be the simultaneous random encoding method, which requires only $2N_\omega$ wavefield propagations; simultaneous plane-wave encoding is also relatively efficient, considering its ability to get rid of the cross-talk. If the acquisition geometry is not OBC or land geometry, it would be efficient to use the receiver-side random encoding method; its cost is comparable to that of the shot-profile migration. Besides needing fewer wavefield propagations, phase-encoding methods do not require to save any Green's functions on the hard disk, which is good news for practical applications, since the size of the Green's functions ($N_x N_y N'_x N'_y N'_z N_\omega$) by direct computation can easily reach a ridiculously large number.

NUMERICAL EXAMPLES

In this section, I show several numerical examples for two different velocity models. The first is a simple constant-velocity model, which I use to verify the proposed

algorithms for Hessian computation; the second is the more complicated Sigsbee2A velocity model. Because of the complex salt body and limited acquisition geometry, there are shadow zones under the salt where conventional wave-equation migration algorithms often fail to produce reliable images. Therefore, it is useful to show how inversion by using the phase-encoded Hessian can improve the final image.

Verification of the algorithm: A constant velocity model

I verify the proposed phase-encoding algorithms on a constant velocity model ($v = 2000$m/s) for different acquisition geometries. Figure 1 shows the diagonal of the Hessian (when $\mathbf{x}_p = \mathbf{x}_q$). The diagonal of the Hessian is computed using different methods, with an acquisition geometry containing only one shot located at -600m and two receivers located at 600m and 1200m on the surface. The frequency band of the seismic experiment is from 5 Hz to 35 Hz, and all the frequencies are used to generate the following results. Figure 1(a) is the exact diagonal of Hessian $H(\mathbf{x}_p, \mathbf{x}_p)$ uncontaminated by any cross-talk artifacts. Figure 1(b) is obtained by directly implementing equation 9. No weighting functions are applied ($\alpha_k(\omega) = 1$), so the result is contaminated by strong cross-talk, which can be easily identified as the vertical stripes on the right side of the image. Figure 1(c) is obtained by using plane-wave phase encoding after stacking 61 receiver-side-encoded plane waves. It successfully removes the cross-talk, and Figure 1(c) looks very similar to Figure 1(a). Figure 1(d) shows the result obtained by using the random phase encoding method. The cross-talk is greatly reduced by the random phase functions, but is not completely attenuated. As I show later, the result of random phase encoding can be improved by stacking more receivers or shots.

Figure 2 shows the Hessian with off-diagonals (with size 21×21) at the image point $x = 680$m, $z = 800$m. The acquisition geometry is the same as that in Figure 1. The horizontal and vertical axes in Figure 2 show the horizontal and vertical offsets away from that image point. Figure 2(a) is the exact Hessian; Figure 2(b) shows the Hessian with strong cross-talk; Figures 2(c) and (d) show the results obtained with plane-wave phase encoding and random phase encoding respectively. Both phase-encoding schemes successfully remove the cross-talk shown in Figure 2(b).

In the next example, I slightly change the acquisition geometry used in the previous example from two receivers to 401 receivers. The receivers range from -2000m to 2000m, with a spacing of 10m. Once again, Figure 3 shows the diagonal of the Hessian operator, while Figure 4 illustrates the off-diagonals at the image point $x = 680$m, $z = 800$m. The results shown in Figure 3(c) and Figure 4(c) are obtained by using receiver-side plane-wave phase encoding, which perfectly removes the cross-talk. Figure 3(d) and Figure 4(d) show the results of random phase encoding. The cross-talk in the bottom left and right corners is also well removed. Also note that some random background noise has been introduced (Figure 3(d)).

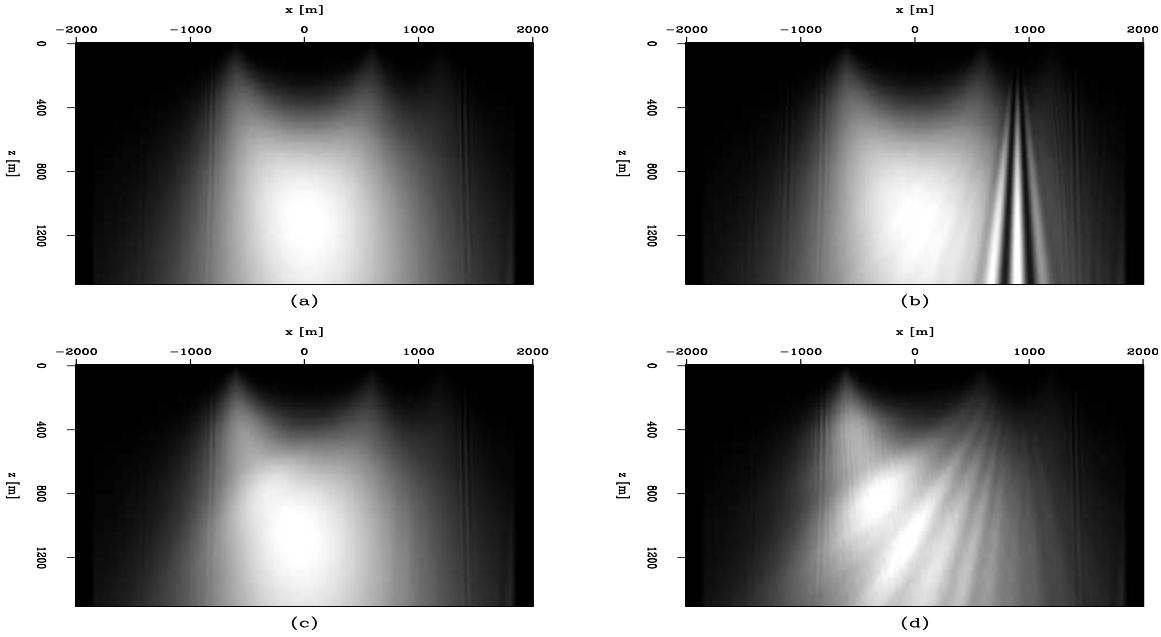

Figure 1: Diagonal of the Hessian for a constant-velocity model with only one shot and two receivers. (a) shows the exact diagonal of the Hessian obtained by directly implementing equation 8; (b) is obtained by using equation 9, and it is contaminated by strong cross-talk, which can be easily identified as the vertical stripes in the result; (c) is obtained by using plane-wave phase-encoding with 61 receiver-side-encoded plane waves stacked together to generate the result; the cross-talk is successfully removed; (d) is obtained by using the random phase-encoding; the cross-talk is dispersed, and the result contains less cross-talk. [**ER**]

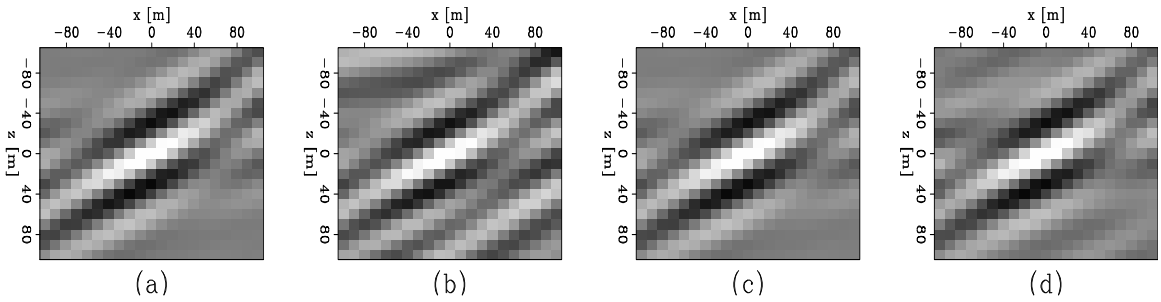

Figure 2: The Hessian operator for image point $x = 680$m, $z = 800$m with the same acquisition geometry as in Figure 1. The size of the Hessian operator is 21×21. Panel (a) shows the exact Hessian operator, free of cross-talk; (b) is obtained by using equation 9, and is contaminated by strong cross-talk, which can be easily identified by comparing with (a); (c) is obtained by using plane-wave phase-encoding with 61 receiver-side-encoded plane waves stacked together to generate the result; the cross-talk is successfully removed; (d) is obtained by using random phase-encoding, which also successfully removes the cross-talk. [**ER**]

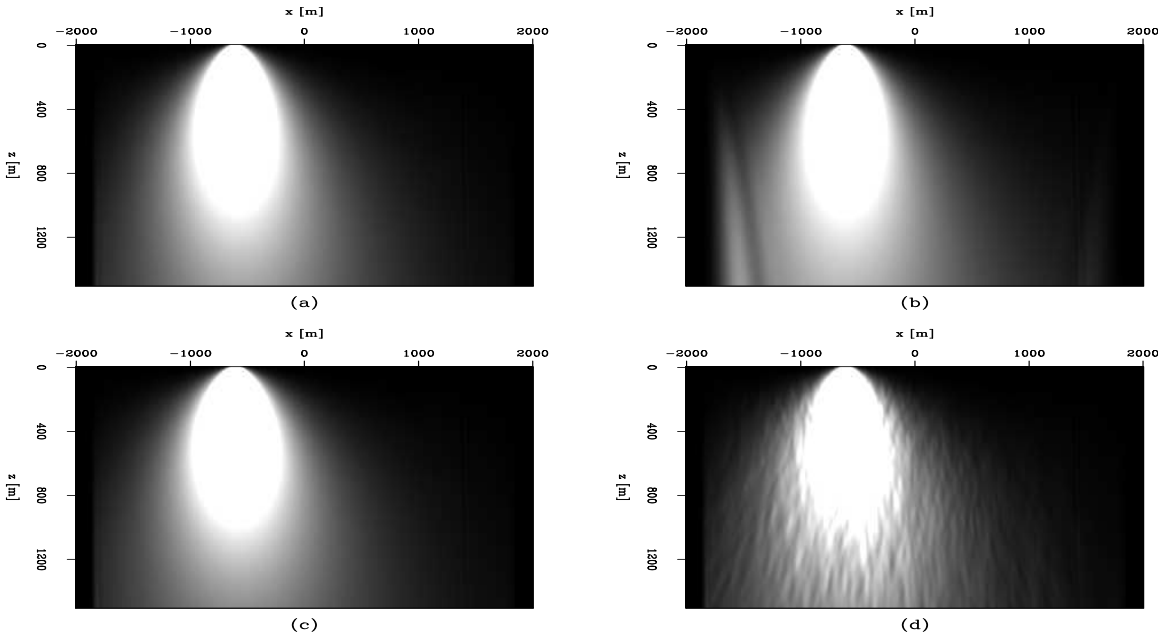

Figure 3: Diagonal of the Hessian for a constant velocity model with only one shot but 401 receivers. Panel (a) shows the exact diagonal of the Hessian obtained by directly implementing equation 8; (b) is obtained by using equation 9, and is contaminated by strong cross-talk, which can be easily identified by comparing with (a); (c) is obtained by using plane-wave phase-encoding with 61 receiver-side-encoded plane waves stacked together; the cross-talk is successfully removed; (d) is obtained by using the random phase-encoding method; the cross-talk in the corners is also successfully removed, but random background noise is introduced. [**ER**]

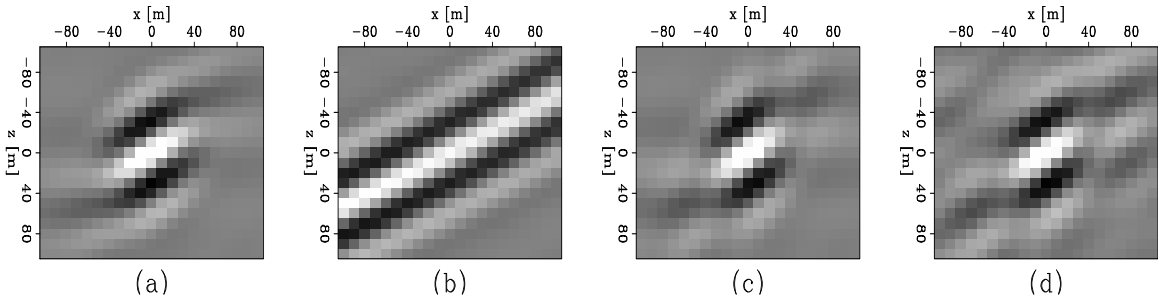

Figure 4: The Hessian operators for image point at $x = 680$m and $z = 800$m, with the same acquisition geometry as in Figure 3. The size of the Hessian operator is 21×21. Panel (a) shows the Hessian operator obtained by using the exact equation 8; it is free of cross-talks; (b) is obtained by using equation 9, and is contaminated by strong cross-talk, which can be easily identified by comparing with (a), note the cross-talk significantly influences the illumination pattern for that image point; (c) is obtained by using the plane-wave phase-encoding method with 61 receiver-side-encoded plane waves stacked together to generate the result; the cross-talk is successfully removed; (d) is obtained by using the random phase-encoding method, which also successfully removes the cross-talk. [**ER**]

Inversion with the phase-encoded Hessian: Sigsbee2A

To demonstrate the power of inversion, I apply the model-space inversion approach to the Sigsbee2A model. The explicit Hessian operator is computed using the random phase-encoding method with the frequency band from 5 Hz to 35 Hz, equivalent to that of the migrated image $\mathbf{m}_{mig}$. I apply Two different strategies: the first is to compute only the diagonal of the Hessian operator and use it to normalize the migrated image; the other is to compute a limited number of Hessian off-diagonals, and then use the linear conjugate gradient method to invert the reflectivity $\mathbf{m}$.

Figure 5 shows the diagonal of the Hessian using random phase encoding. Note the uneven illumination caused by the complex salt body and limited acquisition geometry. For comparison, Figure 6 shows the source intensity (SI), computed using the following equation:

$$\begin{aligned} H(\mathbf{x}_p,\mathbf{x}_p) \approx H_{SI}(\mathbf{x}_p,\mathbf{x}_p) &= \sum_{\omega}\omega^4\sum_{i=1}^{N}|f_s(\omega)|^2 G(\mathbf{s}_i,\mathbf{x}_p,\omega)G'(\mathbf{s}_i,\mathbf{x}_p,\omega) \\ &= \sum_{\omega}\omega^4\sum_{i=1}^{N}|f_s(\omega)|^2 |G(\mathbf{s}_i,\mathbf{x}_p,\omega)|^2. \end{aligned} \tag{30}$$

Comparing equation 30 with equation 8, $H_{SI}(\mathbf{x}_p,\mathbf{x}_p)$ is a crude approximation to the exact diagonal of Hessian, because it assumes the constant receiver-side Green's functions and ignores the effects of the limited receiver arrays. It over-estimates the total energy that enters the earth and returns to be recorded by the receivers. That is why Figure 6 shows a better, but inaccurate, illumination coverage below the salt.

Figure 7 shows the conventional shot-profile migrated image, where the shadow zones below the salt are easily identified; Figure 8 shows the result of normalizing the migrated image with the diagonal of the Hessian shown in Figure 5. For comparison, Figure 9 shows the result of normalizing the migrated image with the source intensity shown in Figure 6. Figure 8 shows slightly more balanced amplitude across the section than Figure 9, especially in areas below the salt. This is because Figure 5 takes the limited receiver arrays into consideration, and hence better predicts the illumination pattern in the subsurface.

Figure 10 shows the Hessian operator obtained by random phase encoding for a particular region of interest under the salt: (a) shows the diagonal of the Hessian; (b) is obtained by convolving the Hessian operator (with a size 21×21) with a collection of point scatters in the model space. It demonstrates the varying shapes and non-stationarities of the Hessian operators across the model space. Note that in well-illuminated areas, the Hessian operator is well focused, while in poorly illuminated areas, the Hessian operator has a preferred dipping orientation, which means these image points are illuminated at only a few dip angles.

Figure 11 shows the comparison between migration and inversion: (a) is the migrated image, and (b) is the inverted image obtained using the randomly phase-encoded Hessian operator. The result is obtained after 20 iterations of the linear

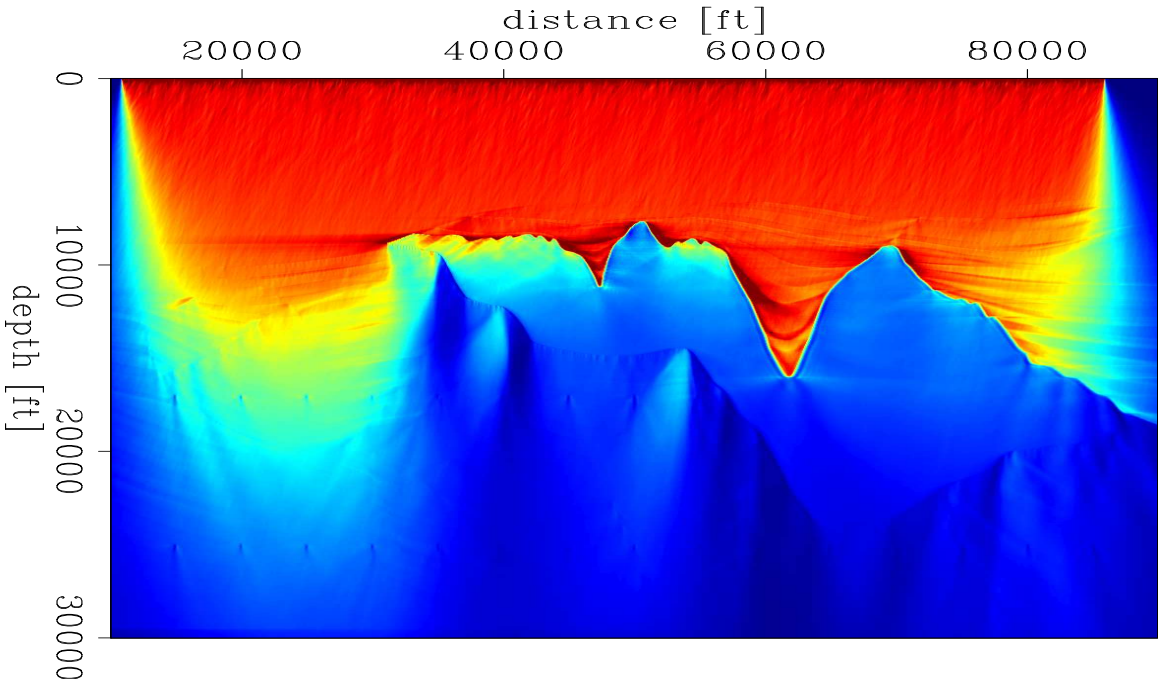

Figure 5: Diagonal of Hessian for the Sigsbee2A model. The Hessian is obtained by using random phase encoding, which takes the limited receiver array into consideration. The result shows the Hessian for the entire frequency band (5 Hz - 35 Hz). [**CR**]

conjugate-gradient method. Figure 12 plots the residuals as a function of iteration number, the residual converges after about 12 iterations. In the inversion result, the vertical resolution is greatly enhanced; the shadow zones that in the migrated image are now filled in with structures; the sediments and the large dipping fault extend closer to the salt body. However, the inversion result also shows increased noise, which might be caused by the null space or the random noise introduced in the randomly phase-encoded Hessian, or both. To suppress the noise, a proper regularization term can be introduced in the inversion process.

CONCLUSIONS

I introduce a method based on phase encoding that allows efficient computation of the explicit Hessian operator. The proposed algorithm closely resembles shot-profile migration, except that a slightly different imaging condition is used, so that no Green's functions need to be pre-computed and saved on disk; hence, Hessians with larger model spaces and more frequencies can be obtained. However, this method also generates undesired cross-talk. I examine plane-wave phase encoding and random phase encoding to attenuate the cross-talk. Numerical examples demonstrate that these two phase-encoding schemes work well in suppressing the cross-talk. The inversion ex-

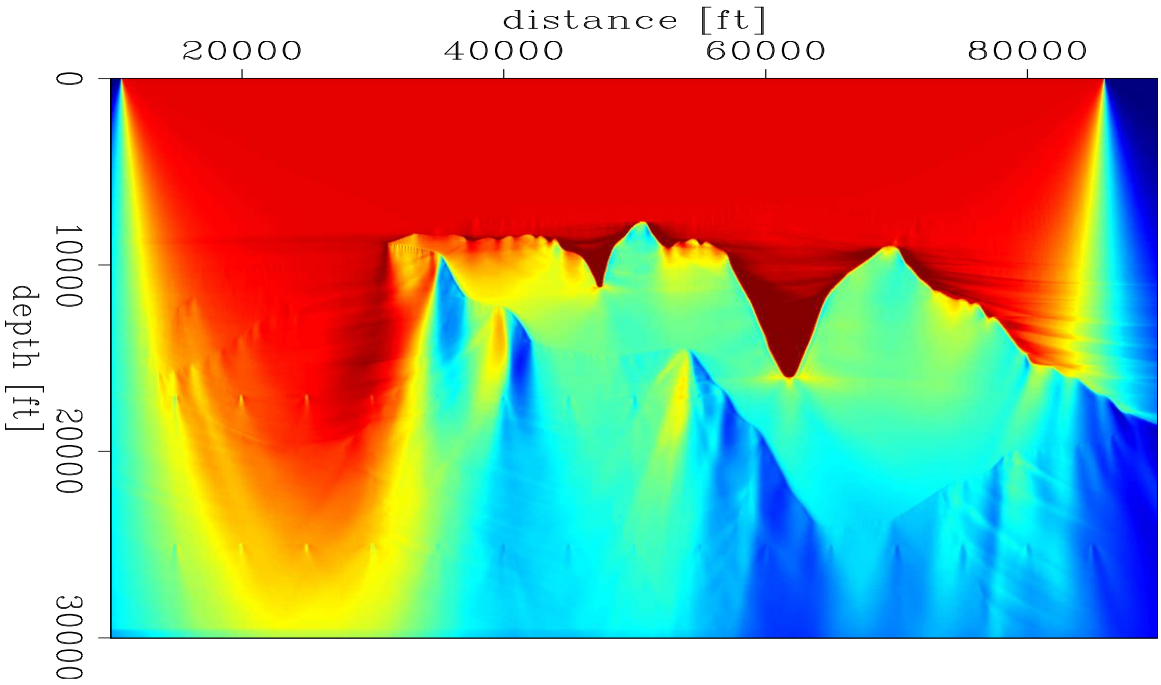

Figure 6: Source intensity for the Sigsbee2A model obtained by using equation 30, which assumes the receiver-side Green's functions to be constant; it ignores the effects of limited receiver array and over-estimates the total energy that enters the earth and returns to be recorded by the receivers. [**CR**]

amples of using randomly phase-encoded Hessian on the Sigsbee2A model also show promising results.

ACKNOWLEDGMENT

I would like to thank Alejandro Valenciano for helpful discussions on the inversion part.

REFERENCES

Beylkin, G., 1985, Imaging of discontinuities in the inverse scattering problem by inversion of a causal generalized radon transform: J. Math. Phys., **26**, 99–108.

Chavent, G. and R.-E. Plessix, 1999, An optimal true-amplitude least-squares prestack depth-migration operator: Geophysics, **64**, 508–515.

Claerbout, J. F., 1971, Towards a unified theory of reflector mapping: Geophysics, **36**, 467–481.

Clapp, M. L., 2005, Imaging under salt: Illumination compensation by regularized inversion, *in* Ph.D. Thesis, Stanford University.

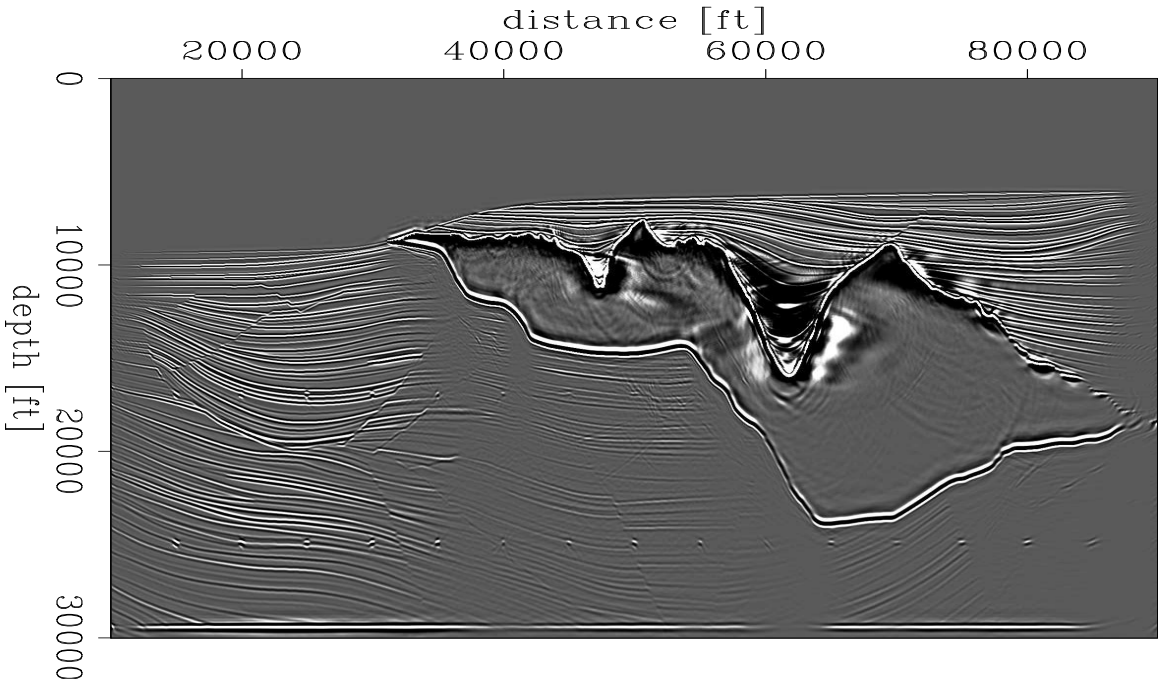

Figure 7: Conventional shot-profile migration result of Sigsbee2A model. Note the shadow zones under the salt. [**CR**]

Lailly, P., 1983, The seismic inverse problem as a sequence of before stack migration: Proc. Conf. on Inverse Scattering, Theory and Applications, Expanded Abstracts, Philadelphia, SIAM.

Liu, F., D. W. Hanson, N. D. Whitmore, R. S. Day, and R. H. Stolt, 2006, Toward a unified analysis for source plane-wave migration: Geophysics, **71**, S129–S139.

Nemeth, T., C. Wu, and G. Schuster, 1999, Least-squares migration of incomplete reflection data: Geophysics, **64**, 208–221.

Plessix, R.-E. and W. A. Mulder, 2004, Frequency-domain finite-difference amplitude-preserving migration: Geophys. J. Int., **157**, 975–987.

Pratt, R. G., C. Shin, and G. J. Hicks, 1998, Gauss-newton and full newton methods in frequency-space seismic waveform inversion: Geophys. J. Int., **133**, 341–362.

Romero, L. A., D. C. Ghiglia, C. C. Ober, and S. A. Morton, 2000, Phase encoding of shot records in prestack migration: Geophysics, **65**, 426–436.

Tarantola, A., 1984, Inversion of seismic reflection data in the acoustic approximation: Geophysics, **49**, 1259–1266.

Valenciano, A. A., B. Biondi, and A. Guitton, 2006, Target-oriented wave-equation inversion: Geophysics, **71**, A35–A38.

Whitmore, N. D., 1995, An imaging hierarchy for common angle plane wave seismograms, *in* Ph.D. thesis, University of Tulsa.

Yu, J., J. Hu, G. T. Schuster, and R. Estill, 2006, Prestack migration deconvolution: Geophysics, **71**, S53–S62.

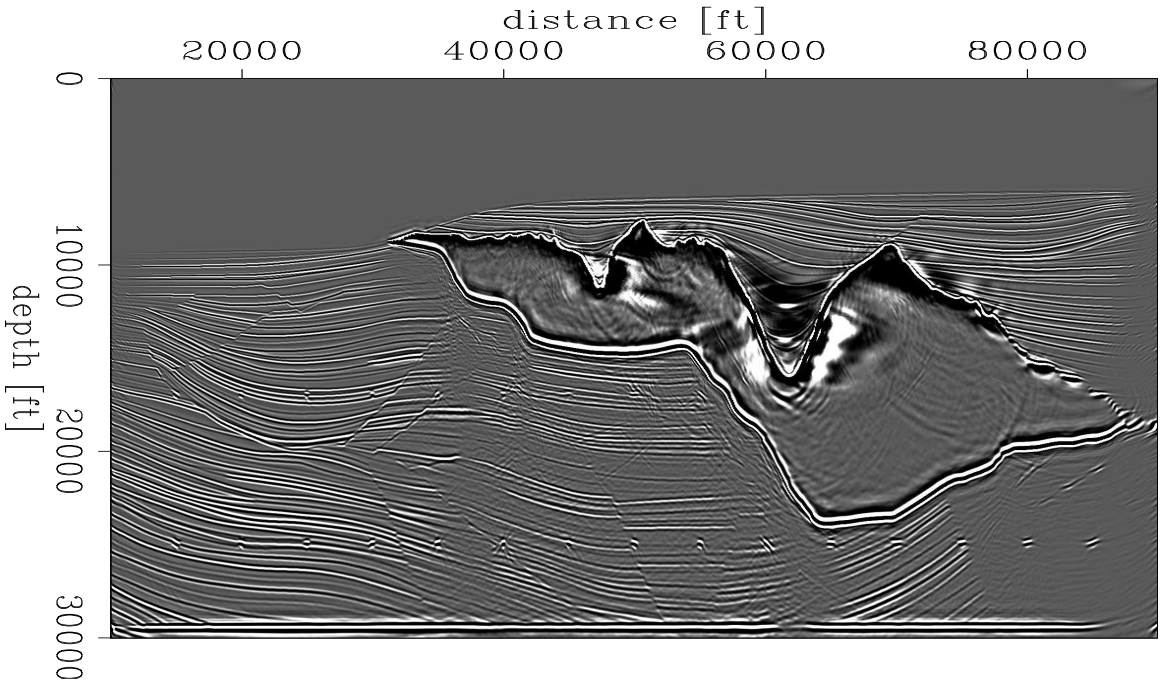

Figure 8: The migrated image (Figure 7) is normalized by the diagonal of the Hessian shown in Figure 5. [**CR**]

APPENDIX A

This appendix derives the Hessian operator of a linear least-squares functional. Let us start with the objective function

$$F(\mathbf{m}) = \frac{1}{2} \sum_{\omega} \sum_{k=1}^{M} \sum_{i=1}^{N} \left| d(\mathbf{r}_k, \mathbf{s}_i, \omega) - d_{obs}(\mathbf{r}_k, \mathbf{s}_i, \omega) \right|^2 , \tag{A-1}$$

where the forward modeling operator is defined by

$$d(\mathbf{r}_k, \mathbf{s}_i, \omega) = \omega^2 \sum_{l=1}^{L} f_s(\omega) G(\mathbf{s}_i, \mathbf{x}_l, \omega) G(\mathbf{x}_l, \mathbf{r}_k, \omega) m(\mathbf{x}_l). \tag{A-2}$$

The first-order partial derivative of the above objective function with respect to the model parameter (the gradient) is:

$$\frac{\partial F(\mathbf{m})}{\partial m(\mathbf{x}_p)} = \sum_{\omega} \omega^2 \sum_{i=1}^{N} \sum_{k=1}^{M} \left(d'(\mathbf{r}_k, \mathbf{s}_i, \omega) - d'_{obs}(\mathbf{r_k}, \mathbf{s_i}, \omega) \right) f_s(\omega) G(\mathbf{s}_i, \mathbf{x}_p, \omega) G(\mathbf{x}_p, \mathbf{r}_k, \omega). \tag{A-3}$$

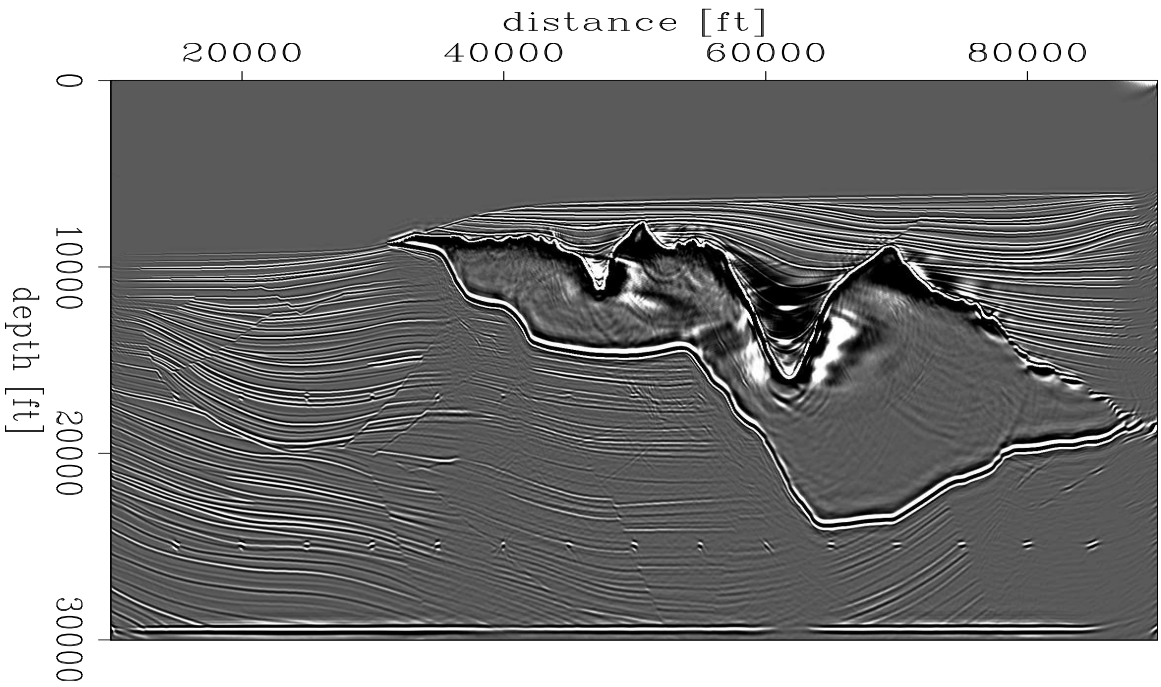

Figure 9: The migrated image (Figure 7) is normalized by the source intensity shown in Figure 6. [**CR**]

The Hessian is then obtained by taking the second-order partial derivatives of the objective function with respect to the model parameters:

$$\begin{aligned} H(\mathbf{x}_p, \mathbf{x}_q) &= \frac{\partial^2 F(\mathbf{m})}{\partial m(\mathbf{x}_p) \partial m(\mathbf{x}_q)} \\ &= \sum_{\omega} \omega^4 \sum_{i=1}^{N} |f_s(\omega)|^2 G(\mathbf{s}_i, \mathbf{x}_p, \omega) G'(\mathbf{s}_i, \mathbf{x}_q, \omega) \sum_{k=1}^{M} G(\mathbf{x}_p, \mathbf{r}_k, \omega) G'(\mathbf{x}_q, \mathbf{r}_k, \omega). \end{aligned} \tag{A-4}$$

We can further assume that the reciprocity holds, such that:

$$G(\mathbf{x}, \mathbf{y}, \omega) = G(\mathbf{y}, \mathbf{x}, \omega). \tag{A-5}$$

Therefore, the Hessian can be rewritten as follows:

$$H(\mathbf{x}_p, \mathbf{x}_q) = \sum_{\omega} \omega^4 \sum_{i=1}^{N} |f_s(\omega)|^2 G(\mathbf{s}_i, \mathbf{x}_p, \omega) G'(\mathbf{s}_i, \mathbf{x}_q, \omega) \sum_{k=1}^{M} G(\mathbf{r}_k, \mathbf{x}_p, \omega) G'(\mathbf{r}_k, \mathbf{x}_q, \omega). \tag{A-6}$$

Equation A-6 is equivalent to equation 8.

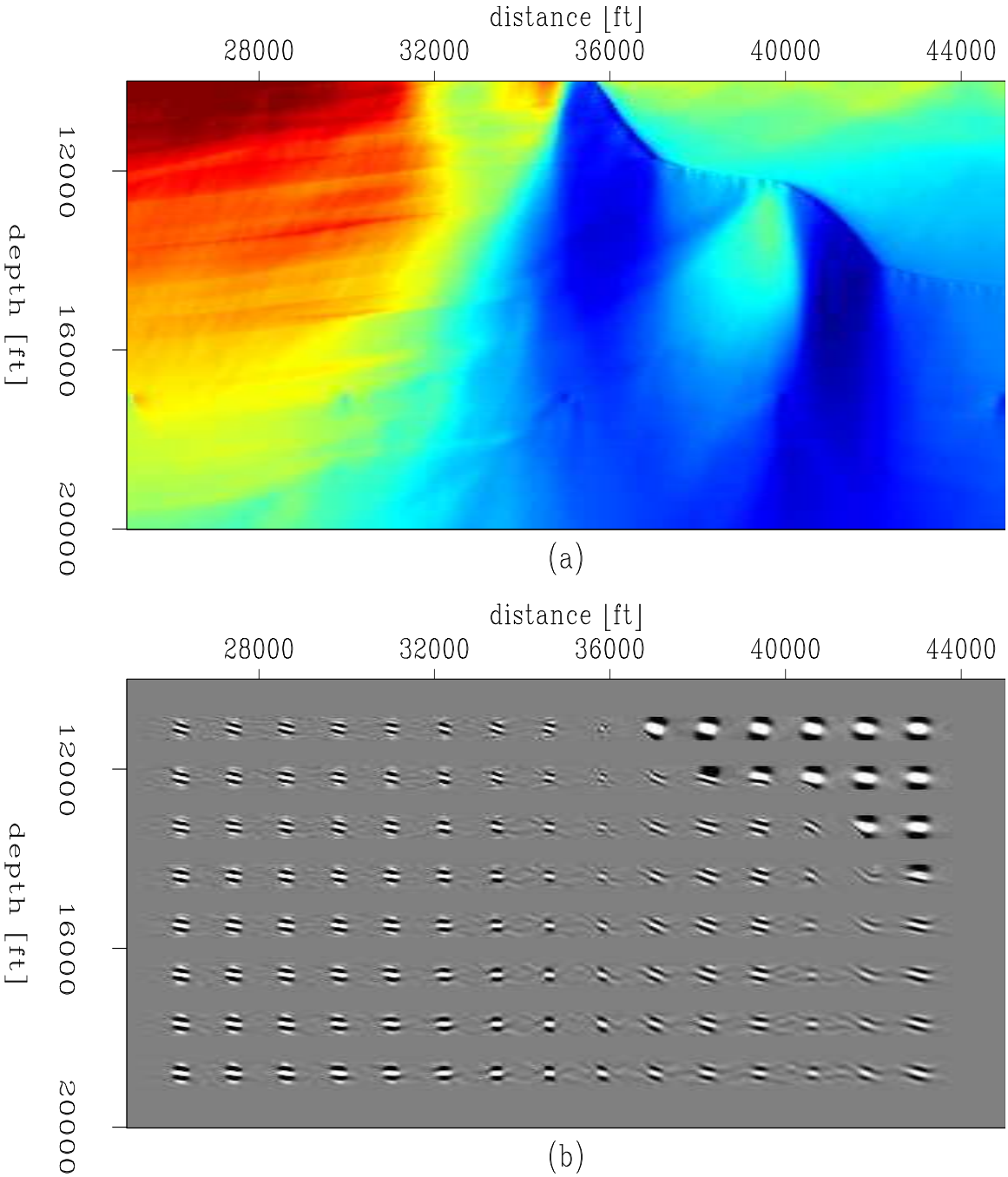

Figure 10: Randomly phase-encoded Hessian operators for Sigsbee2A. Panel (a) shows the diagonal of the randomly phase-encoded Hessian for a particular region of interest under the salt, note the uneven illumination due the complex salt body and limited acquisition geometry; (b) shows the result by convolving the Hessian operator (with a size 21×21) with a collection of point scatters, it demonstrates the varying shapes of the operators. [**CR**]

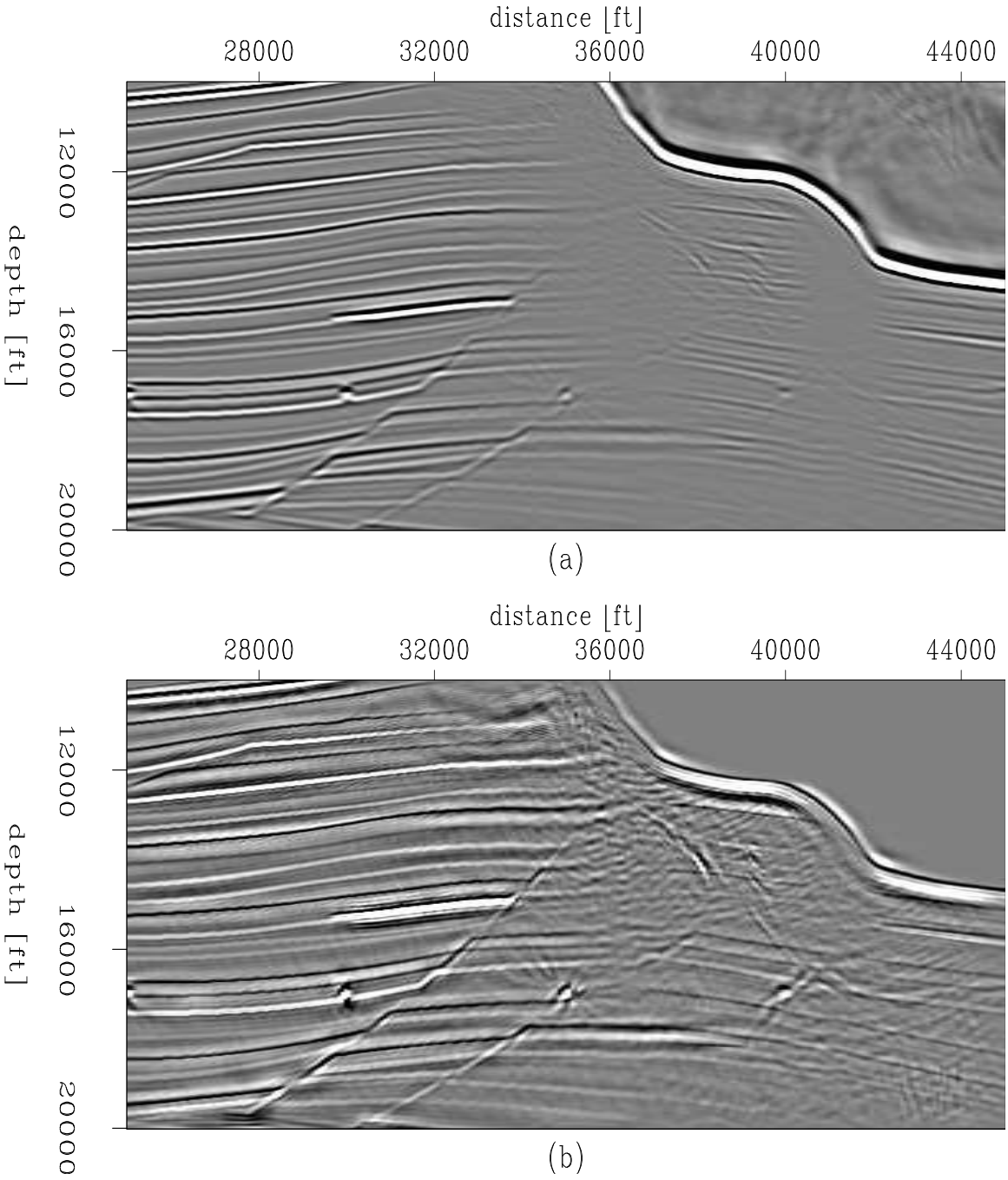

Figure 11: Comparison between migration and inversion. Panel (a) shows the conventional shot-profile migration result; (b) shows the inversion result using the 21×21 Hessian operators obtained by using the random phase-encoding method. [**CR**]

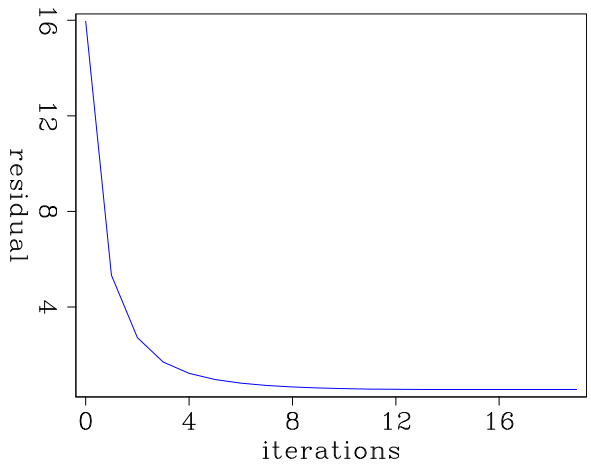

Figure 12: Residual vs. number of iterations for the Sigsbee2A model; the inversion converges after about 12 iterations. [**CR**]

APPENDIX B

This appendix demonstrates that the receiver-side plane-wave-encoded Hessian $\tilde{H}(\mathbf{x}_p, \mathbf{x}_q, p_r)$ converges to the exact Hessian $H(\mathbf{x}_p, \mathbf{x}_q)$ by stacking over receiver ray parameters. By using the weighting functions defined in equation 23, the approximate Hessian for a single p_r takes the form:

$$\begin{aligned}\tilde{H}(\mathbf{x}_p, \mathbf{x}_q, p_r) &= \sum_{\omega} \omega^4 \sum_{i=1}^{N} |f_s(\omega)|^2 A_r^2(\omega) G(\mathbf{s}_i, \mathbf{x}_p, \omega) G'(\mathbf{s}_i, \mathbf{x}_q, \omega) \times \\ &\quad \sum_{u=1}^{M} G(\mathbf{r}_u, \mathbf{x}_p, \omega) \mathrm{e}^{\iota\omega p_r(\mathbf{r}_u - \mathbf{r}_0)} \sum_{v=1}^{M} G'(\mathbf{r}_v, \mathbf{x}_q, \omega) \mathrm{e}^{-\iota\omega p_r(\mathbf{r}_v - \mathbf{r}_0)}. \quad \text{(B-1)}\end{aligned}$$

If we stack over p_r from $-\infty$ to $+\infty$, we have

$$\begin{aligned}\sum_{p_r=-\infty}^{+\infty} \tilde{H}(\mathbf{x}_p, \mathbf{x}_q, p_r) &= \sum_{p_r=-\infty}^{+\infty} \sum_{\omega} \omega^4 \sum_{i=1}^{N} |f_s(\omega)|^2 A_r^2(\omega) G(\mathbf{s}_i, \mathbf{x}_p, \omega) G'(\mathbf{s}_i, \mathbf{x}_q, \omega) \times \\ &\quad \sum_{u=1}^{M} G(\mathbf{r}_u, \mathbf{x}_p, \omega) \mathrm{e}^{\iota\omega p_r(\mathbf{r}_u - \mathbf{r}_0)} \sum_{v=1}^{M} G'(\mathbf{r}_v, \mathbf{x}_q, \omega) \mathrm{e}^{-\iota\omega p_r(\mathbf{r}_v - \mathbf{r}_0)} \\ &= \sum_{\omega} \omega^4 \sum_{i=1}^{N} |f_s(\omega)|^2 A_r^2(\omega) G(\mathbf{s}_i, \mathbf{x}_p, \omega) G'(\mathbf{s}_i, \mathbf{x}_q, \omega) \times \\ &\quad \sum_{u=1}^{M} G(\mathbf{r}_u, \mathbf{x}_p, \omega) \sum_{v=1}^{M} G'(\mathbf{r}_v, \mathbf{x}_q, \omega) \sum_{p_r=-\infty}^{+\infty} \mathrm{e}^{-\iota\omega p_r(\mathbf{r}_v - \mathbf{r}_u)}. \quad \text{(B-2)}\end{aligned}$$

Note that

$$\sum_{p_r=-\infty}^{+\infty} \mathrm{e}^{-\iota\omega p_r(\mathbf{r}_v - \mathbf{r}_u)} \approx \frac{1}{|\omega|} \delta(\mathbf{r}_v - \mathbf{r}_u). \quad \text{(B-3)}$$

If we choose the real function $A_r(\omega)$ such that it satisfies

$$\frac{A_r^2(\omega)}{|\omega|} = 1, \tag{B-4}$$

then we get

$$\begin{aligned}
\sum_{p_r=-\infty}^{+\infty} \tilde{H}(\mathbf{x}_p, \mathbf{x}_q, p_r) &= \sum_{\omega} \omega^4 \sum_{i=1}^{N} |f_s(\omega)|^2 \frac{A_r^2(\omega)}{|\omega|} G(\mathbf{s}_i, \mathbf{x}_p, \omega) G'(\mathbf{s}_i, \mathbf{x}_q, \omega) \times \\
&\quad \sum_{u=1}^{M} G(\mathbf{r}_u, \mathbf{x}_p, \omega) \sum_{v=1}^{M} G'(\mathbf{r}_v, \mathbf{x}_q, \omega) \delta(\mathbf{r}_v - \mathbf{r}_u) \\
&= \sum_{\omega} \omega^4 \sum_{i=1}^{N} |f_s(\omega)|^2 G(\mathbf{s}_i, \mathbf{x}_p, \omega) G'(\mathbf{s}_i, \mathbf{x}_q, \omega) \times \\
&\quad \sum_{u=1}^{M} G(\mathbf{r}_u, \mathbf{x}_p, \omega) G'(\mathbf{r}_u, \mathbf{x}_q, \omega) \\
&= H(\mathbf{x}_p, \mathbf{x}_q).
\end{aligned} \tag{B-5}$$

APPENDIX C

This appendix demonstrates that the simultaneously plane-wave-encoded Hessian $\tilde{\tilde{H}}(\mathbf{x}_p, \mathbf{x}_q, p_s, p_r)$ converges to the exact Hessian $H(\mathbf{x}_p, \mathbf{x}_q)$ by stacking over both source and receiver ray parameters. The simultaneously plane-wave-encoded Hessian takes the form

$$\begin{aligned}
\tilde{\tilde{H}}(\mathbf{x}_p, \mathbf{x}_q, p_s, p_r) &= \sum_{\omega} \omega^4 |f_s(\omega)|^2 A_s^2(\omega) A_r^2(\omega) \times \\
&\quad \sum_{i=1}^{N} G(\mathbf{s}_i, \mathbf{x}_p, \omega) \mathrm{e}^{\iota\omega p_s(\mathbf{s}_i - \mathbf{s}_0)} \sum_{j=1}^{N} G'(\mathbf{s}_j, \mathbf{x}_q, \omega) \mathrm{e}^{-\iota\omega p_s(\mathbf{s}_j - \mathbf{s}_0)} \times \\
&\quad \sum_{u=1}^{M} G(\mathbf{r}_u, \mathbf{x}_p, \omega) \mathrm{e}^{\iota\omega p_r(\mathbf{r}_u - \mathbf{r}_0)} \sum_{v=1}^{M} G'(\mathbf{r}_v, \mathbf{x}_q, \omega) \mathrm{e}^{-\iota\omega p_r(\mathbf{r}_v - \mathbf{r}_0)}.
\end{aligned} \tag{C-1}$$

By stacking over p_s and p_r, we get

$$\begin{aligned}\sum_{p_s=-\infty}^{+\infty}\sum_{p_r=-\infty}^{+\infty}\tilde{\tilde{H}}(\mathbf{x}_p,\mathbf{x}_q,p_s,p_r) &= \sum_{\omega}\omega^4|f_s(\omega)|^2A_s^2(\omega)A_r^2(\omega)\times \\ &\sum_{i=1}^{N}G(\mathbf{s}_i,\mathbf{x}_p,\omega)\sum_{j=1}^{N}G'(\mathbf{s}_j,\mathbf{x}_q,\omega)\sum_{p_s=-\infty}^{+\infty}\mathrm{e}^{-\iota\omega p_s(\mathbf{s}_j-\mathbf{s}_i)}\times \\ &\sum_{u=1}^{M}G(\mathbf{r}_u,\mathbf{x}_p,\omega)\sum_{v=1}^{M}G'(\mathbf{r}_v,\mathbf{x}_q,\omega)\sum_{p_r=-\infty}^{+\infty}\mathrm{e}^{-\iota\omega p_r(\mathbf{r}_v-\mathbf{r}_u)}.\end{aligned} \tag{C-2}$$

Once again note that

$$\sum_{p_r=-\infty}^{+\infty}\mathrm{e}^{-\iota\omega p_s(\mathbf{s}_j-\mathbf{s}_i)} \approx \frac{1}{|\omega|}\delta(\mathbf{s}_j-\mathbf{s}_i) \tag{C-3}$$

$$\sum_{p_r=-\infty}^{+\infty}\mathrm{e}^{-\iota\omega p_r(\mathbf{r}_v-\mathbf{r}_u)} \approx \frac{1}{|\omega|}\delta(\mathbf{r}_v-\mathbf{r}_u). \tag{C-4}$$

If we choose real functions $A_s(\omega)$ and $A_r(\omega)$ such that they satisfy

$$\frac{A_s^2(\omega)}{|\omega|} = 1 \tag{C-5}$$

$$\frac{A_r^2(\omega)}{|\omega|} = 1, \tag{C-6}$$

then we get

$$\begin{aligned}\sum_{p_s=-\infty}^{+\infty}\sum_{p_r=-\infty}^{+\infty}\tilde{\tilde{H}}(\mathbf{x}_p,\mathbf{x}_q,p_s,p_r) &= \sum_{\omega}\omega^4|f_s(\omega)|^2\frac{A_s^2(\omega)}{|\omega|}\frac{A_r^2(\omega)}{|\omega|}\times \\ &\sum_{i=1}^{N}G(\mathbf{s}_i,\mathbf{x}_p,\omega)\sum_{j=1}^{N}G'(\mathbf{s}_j,\mathbf{x}_q,\omega)\delta(\mathbf{s}_j-\mathbf{s}_i)\times \\ &\sum_{u=1}^{M}G(\mathbf{r}_u,\mathbf{x}_p,\omega)\sum_{v=1}^{M}G'(\mathbf{r}_v,\mathbf{x}_q,\omega)\delta(\mathbf{r}_v-\mathbf{r}_u)\times \\ &= \sum_{\omega}\omega^4|f_s(\omega)|^2\sum_{i=1}^{N}G(\mathbf{s}_i,\mathbf{x}_p,\omega)G'(\mathbf{s}_i,\mathbf{x}_q,\omega)\times \\ &\sum_{k=1}^{M}G(\mathbf{r}_k,\mathbf{x}_p,\omega)G'(\mathbf{r}_k,\mathbf{x}_q,\omega) \\ &= H(\mathbf{x}_p,\mathbf{x}_q).\end{aligned} \tag{C-7}$$